Organic Electronics 14 (2013) 934–941

Contents lists available at SciVerse ScienceDirect

Organic Electronics

journal homepage: www.elsevier.com/locate/orgel

Intermolecular interactions in organic semiconductors based on annelated β-oligothiophenes and their effect on the performance of organic field-effect transistors

Jianwu Shi [a,*], Li Xu [b], Yabo Li [a], Ming Jia [a], Yuhe Kan [c,*], Hua Wang [a,*]

[a] Key Lab for Special Functional Materials of Ministry of Education, Henan University, Kaifeng 475004, China
[b] College of Chemistry and Chemical Engineering, Henan University, Kaifeng 475004, China
[c] Jiangsu Province Key Laboratory for Chemistry of Low Dimensional Materials, School of Chemistry and Chemical Engineering, Huaiyin Normal University, Huanan 223300, China

ARTICLE INFO

Article history:
Received 16 September 2012
Received in revised form 30 December 2012
Accepted 5 January 2013
Available online 30 January 2013

Keywords:
Annelated β-oligothiophene
Single crystal
Intermolecular interaction
Charge transport
Organic field-effect transistors

ABSTRACT

A series of derivatives based on annelated β-oligothiophenes were synthesized and characterized as active layer in organic field-effect transistors (OFETs). Highest field-effect mobility of 0.52 V^{-1} s^{-1} for 2,5-dibiphenyl-dithieno[2,3-*b*:3′,2′-*d*]thiophene (DBP-DTT), 2.2 cm^2 V^{-1} s^{-1} for 2,5-distyryl-dithieno[2,3-*b*:3′,2′-*d*]thiophene (DEP-DTT), and 0.16 cm^2 V^{-1} s^{-1} for 1,4-di[2-dithieno[2,3-*b*:3′,2′-*d*] thiophen-2-yl-vinyl]benzene (DDTT-EP) were obtained, while 2,5-diphenyl-dithieno [2,3-*b*:3′,2′-*d*]thiophene (DP-DTT) presents no field-effect behaviors. Their thermal, optical and electrochemical properties, topographical and X-ray diffraction patterns of films, and the single crystal structures were also investigated. With the end-capping groups changing in these materials, the intermolecular interactions could transform from S–S in DP-DTT to S–C in DBP-DTT, to S–π in DEP-DTT, and to the coexisting of S–S and S–π in DDTT-EP. According to the device performances and the results of transfer integral calculations, it was revealed that S–π intermolecular interaction benefits not only improving the mobility but also reducing the threshold voltage (V_T), while S–S intermolecular interaction is not favorable for promoting the mobility.

1. Introduction

Organic field-effect transistors (OFETs) have attracted particular attention due to their potential advantages of flexibility, large-area, and light-weight [1–5]. Since the first OFETs emerged [6], many efforts have been devoted to improving their performances by adopting new organic semiconductors or optimizing the devices configuration [7–18]. Significant progress has been obtained on their performances, some of which have reached and even exceeded their inorganic counterparts (conventional α-H: silicon-based transistors). Unfortunately, their performances are still lower than that of inorganic devices based on polysilicon and monocrystal silicon. It is well known that inorganic semiconductors are combined with strong covalent bonds, which form netlike structures and provide convenient pathway for carrier transportation. On the contrary, organic semiconductors are coalesced via weak intermolecular interactions, such as Van der Waals interaction, S–S interaction, π–π interaction, and C—H interaction. The discrepancy of combination modes may be a primary factor for the tremendous difference between the mobilities of inorganic and organic semiconductors. Therefore, strengthening the intermolecular interactions may be a possible way to improve the performance of OFETs. However, detailed studies in this domain are rarely reported [19,20]. It is still a significant challenge to investigate the relationship between the intermolecular interactions and the device performance of organic semiconductors.

* Corresponding authors. Tel./fax: +86 378 3881358.
E-mail addresses: jwshi@henu.edu.cn (J. Shi), kyh@hytc.edu.en (Y. Kan), hwang@henu.edu.cn (H. Wang).

1566-1199/$ - see front matter © 2013 Elsevier B.V. All rights reserved.
http://dx.doi.org/10.1016/j.orgel.2013.01.002

Thiophene oligomers have been considered to be promising organic semiconducting materials due to their convenient synthesis, adjustable chemical and physical properties [8–12]. Furthermore, they readily form multiple intermolecular interactions because of the electropositivity of sulfur atoms. Recently, high field-effect mobility (μ) of 2.0 $cm^2 V^{-1} s^{-1}$ was obtained in OFETs based on annelated β-oligothiophenes [19,20]. It has been interpreted that S–S intermolecular interaction can provide another charge transport pathway. In our previous work [21], we have demonstrated that the formation of S–π intermolecular interaction acting as a spring bed benefits the carrier transportation. It is very interesting that the changing of molecular structure in DTT derivatives can bring the transformation of intermolecular interactions from S–S to S–π, and results in the tremendous improvement of the devices performances. Hence, it is necessary to further investigate the relationship between the intermolecular interactions and the device performances.

Herein, we synthesized two new DTT derivatives, namely 2,5-dibiphenyl-dithieno[2,3-*b*:3′,2′-*d*]thiophene (DBP-DTT) and 1,4-di[2-dithieno[2,3-*b*:3′,2′-*d*]thiophen-2-yl-vinyl]benzene (DDTT-EP). A comparison of their single crystal structures and devices performance with those of 2,5-diphenyl-dithieno [2,3-*b*:3′,2′-*d*]thiophene (DP-DTT) and 2,5-distyryl-dithieno[2,3-*b*:3′,2′-*d*]thiophene (DEP-DTT), discloses that: (1) the substitution patterns of end-capping groups play an important role on the intermolecular interactions; (2) S–S intermolecular interaction causes the molecules to adopt a loose arrangement, which is unfavorable for promoting the mobility; (3) the molecules adopt a condensed arrangement via S–π intermolecular interaction, which not only improves the mobility but also reduces the threshold voltage (V_T) of the devices.

2. Experimental

2.1. General

Melting points were obtained on a XT4A (Beijing Sci. & Ins.). EI mass spectra and HRMS were collected on Thermo DSQ II and Waters Micromass Q-Tof MicroTM System, respectively. Thermo-gravimetric analysis (TGA) and differential scanning calorimetry (DSC) were analyzed with EXSTAR 6000 (Seiko) at heating rate of 10 °C min^{-1} under a nitrogen flow. The materials films (50 nm) absorption and photo luminescence (PL) spectra were recorded with PE-Lambda35 and SPEXF212, respectively. Cyclic voltammetry (CV) was performed on a CHI660a electrochemical analyzer with a three-electrode cell in a solution of 0.1 M tetrabutylammonium hexafluorophosphate (Bu_4NPF_6) dissolved in CH_2Cl_2 at a scan rate of 75 mV s^{-1}. The compound films (50 nm) were coated on a platinum electrode (0.6 cm^2) through sublimating the compounds onto the electrode of Pt slice in vacuum at room temperature. A Pt wire was used as the counter electrode and an Ag/AgCl electrode was used as the reference electrode. Its potential was calibrated by the ferrocene/ferrocenium (0.42 V vs Ag/AgCl in CH_2Cl_2). The X-ray crystal structure analyses were made on a Bruker SMART CCD diffractor, using graphite-monochromated Mo K radiation (λ) 0.7107 Å. The AFM topographical images of all films were performed with SPI3800N (Seiko Instruments Inc.) in tapping mode by the probe of 3 N m^{-1} using 2 Hz scan rate at environment. For X-ray diffraction pattern, measurements were performed in θ–2θ continuous scans using X′ Pert Pro MPD (Philips) with Cu Ka radiation.

2.2. Synthesis

The synthetic route of these materials is shown in Scheme 1. Dithieno[2,3-*b*:3′,2′-*d*]thiophene was prepared according to Ref. [22–24]. DP-DTT and DEP-DTT were synthesized according to Ref. [21].

2.2.1. DBP-DTT

A mixture of 2,5-dibromodithieno[2,3-*b*:3′,2′-*d*]thiophene (242 mg, 0.68 mmol), biphenyl-4-ylboronic acid (300 mg, 1.50 mmol, 2.2 equiv), tetrakis(triphenyl-phosphine) palladium (80 mg, 0.068 mmol, 10% equiv), and K_2CO_3 (1.00 g) in THF (15 mL) was refluxed with stirring under argon for 20 h. After cooling, the mixture was quenched with H_2O (50 mL), extracted with $CHCl_3$ (3 × 20 mL) and then washed with H_2O (50 mL). The crude product was sublimated twice to give bright yellow crystals (140 mg, 41.0%). Mp > 300 °C. MS (EI, 70 eV): *m*/*z* = 500.06 (100) [M^+]. HRMS (MALDI) *m*/*z*: calcd for $C_{32}H_{20}S_3$: 500.0727; found: 500.0733. Elemental analysis calcd (%) for $C_{32}H_{20}S_3$: C 76.76, H 4.03, S 19.21; found: C 76.31, H 3.86, S 19.56. IR(KBr): 3447 (Ar–H) cm^{-1}, 760 (C–C) cm^{-1}.

2.2.2. DDTT-EP

Dithieno[2,3-*b*:3′,2′-*d*]thiophene-5-carboxaldehyde (400 mg, 1.79 mmol) and [1,4-phenylenebis(methylene)]-bis(triphenylphosphonium) bromide (697 mg, 0.90 mmol) were dissolved in 24 mL anhydrous methanol under argon. With stirring, a solution of potassium *tert*-butoxide 252 mg (2.24 mmol) in dry methanol (16 mL) was added dropwise. The solution was stirred at 20 °C for 0.5 h and heated to reflux for 48 h. After cooling to ambient temperature, the yellow product was isolated by centrifugation and washed with ethanol. The crude product was sublimated twice to give bright yellow crystals (418 mg, 45%). Mp > 300 °C; MS (EI, 70 eV): *m*/*z* (I%) = 518 ([M^+], 100); HRMS (MALDI) *m*/*z*: calcd for $C_{26}H_{14}S_6$: 517.9420; found: 517.9426; Elemental analysis calcd (%) for $C_{26}H_{14}S_6$: C, 60.19; H, 2.72; S, 37.09; found: C, 60.11; H, 2.44; S, 37.74; IR(KBr): 3077.88, 3016.00 (Ar–H) cm^{-1}, 1618.30 (C═C) cm^{-1}, 946.40 (═C—H) cm^{-1}.

2.3. X-ray single crystal structures analysis

Single crystals of DBP-DTT and DDTT-EP were obtained by accurately controlling the sublimation temperature. The data were collected at 293 K and the structures were refined by full-matrix least-square on F^2. The computations were performed with SHELEX-97 program. All hydrogen atoms were refined anisotropically.

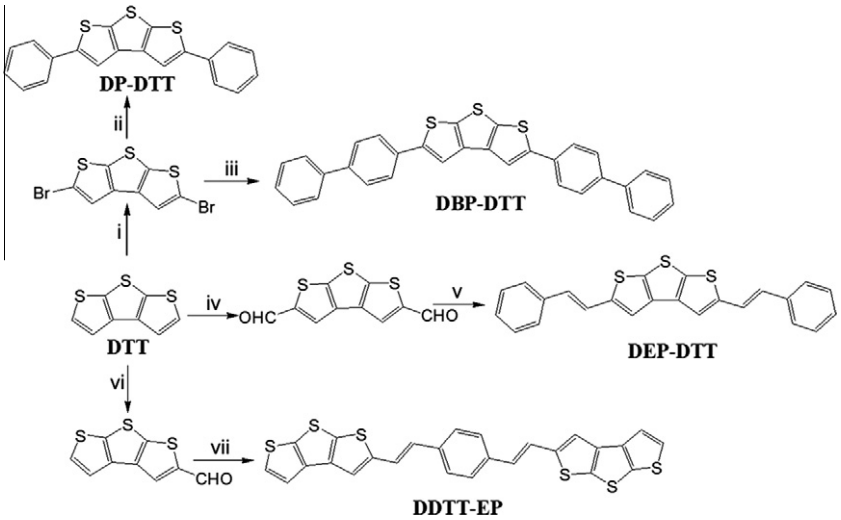

Scheme 1. The synthetic route to DP-DTT, DBP-DTT, DEP-DTT and DDTT-EP. Reagents and conditions: (i) NBS (2.1 equiv) in CHCl3-HOAc (1:1, v/v); (ii) Ph-$B(OH)_2$, $Pd(PPh_3)_4$, K_2CO_3; (iii) Ph-Ph-$B(OH)_2$, $Pd(PPh_3)_4$, K_2CO_3; (iv) LDA (2.2 equiv), DMF (3.0 equiv); (v) $PhCH_2PPh_3Br$, *t*-BuOK; (vi) LDA (1.1 equiv), DMF (2.0 equiv); (vii) $Ph(CH_2PPh_3Br)_2$, *t*-BuOK.

2.3.1. DBP-DTT

$C_{32}H_{20}S_3$, $M = 500.66$; Orthorhombic *Pnma*; crystal size: $0.48 \times 0.44 \times 0.28$ mm; $Z = 4$; cell dimensions: $a = 6.6006(5)$ Å; $b = 48.196(4)$ Å; $c = 7.3292(6)$ Å; $\alpha = 90°$; $\beta = 90°$; $\gamma = 90°$; $V = 2331.6(3)$ Å^3; $\rho = 1.426$ mg cm^{-3}. $F(000) = 1040$, 11694 reflections collected, 2307 independent ($R_{int} = 0.0226$), $R_1 = 0.0496$, $wR_2 = 0.1302$. The CCDC reference number is 859995.

2.3.2. DDTT-EP

$C_{26}H_{14}S_6$, $M = 518.73$; Monoclinic *P21/c*; crystal size: $0.47 \times 0.43 \times 0.12$ mm; $Z = 2$; cell dimensions: $a = 24.96(2)$ Å; $b = 7.627(7)$ Å; $c = 5.820(5)$ Å; $\alpha = 90°$; $\beta = 93.456(18)°$; $\gamma = 90°$; $V = 1106.1(18)$ Å^3; $\rho = 1.448$ mg cm^{-3}. $F(000) = 532$, 4887 reflections collected, 1904 independent ($R_{int} = 0.0769$), $R_1 = 0.1436$, $wR_2 = 0.3870$. The CCDC reference number is 860669.

2.4. Transfer integral calculation

The transfer integral (t) between neighboring molecular pairs in the crystal structure was calculated based on the direct coupling method [25] with ADF program [26] at the M06-2X/TZ2P level of theory. The hybrid meta exchange–correlation functional M06-2X was proved to be suitable for describing noncovalent interactions, such as π–π interaction, C—H···π interaction and so on. [27]

2.5. Devices fabrication

OFETs were fabricated in top contact geometry configuration. A heavily doped, *n*-channel Si wafer, with a 300 or 500 nm thermal oxidation SiO_2 layer as the gate insulator, was used as the gate electrode and substrate. Firstly, the compounds were deposited at different substrate temperature (RT and 70 °C for DP-DTT; RT, 70 °C and 100 °C for DBP-DTT; RT, 70 °C and 100 °C for DEP-DTT; RT, 70 °C and 120 °C for DDTT-EP) with the thickness of 15 nm, respectively. Then, with a shadow mask, the source and drain electrodes with thickness of 50 nm were preceded by thermal evaporating Au. The length (L) and width (W) of channel were 200 μm and 6000 μm, respectively. For electrical characterizations, the devices were transferred to a shield box. The transistors output and transfer characteristics were measured with Keithley 4200 under ambient conditions at room temperature. Carrier mobilities (μ) were calculated in the saturation region by the relationship:

$$\mu = (2I_D L)/[WC_i(V_G - V_T)^2] \quad (1)$$

where I_D is the source–drain saturation current, C_i is the oxide capacitance (7.5 nF cm^{-2}), V_G is the gate voltage, and V_T is the threshold voltage. The latter can be estimated as the intercept of the linear section of the plot of V_G vs $(I_D)^{1/2}$.

3. Results and discussion

3.1. Thermal, optical and electrochemical properties

Thermal properties of these materials were investigated by TGA and DSC (Supplemental information). T_{deg} at 5% weight loss and T_m are shown in Table 1. According to the TGA analysis, all the materials are thermal stable, at least up to 307 °C for DP-DTT under a nitrogen atmosphere. It should be noticed that T_{deg} (422 °C) of DBP-DTT is higher than that of DEP-DTT and DDTT-EP because of the instability of C=C double bond. To explore the correlation between the substitution patterns of aryl groups, energy levels, absorption spectra and electrochemical behaviors of these materials were also measured. Table 1 lists the maximum peak values (λ_{abs}) of these materials films, the levels of optical bandgap (E_g) estimated from the onsets of absorption spectra, and the levels of highest occupied molecular

Table 1
Crystallographic data, thermal and photophysical properties of DTT derivatives.

	Herringbone angle (°)	π–π spacing (Å)	Intermolecular interaction	T_{deg}[a] (°C)	T_m[b] (°C)	λ_{abs}[c] (nm)	E_g[d] (eV)	HOMO[e] (eV)
DP-DTT	79.3	3.578	S–S	307	272	245	2.99	–
DEP-DTT	52.0	2.575	S–π	330	305	306	2.92	4.80
DBP-DTT	38.2	2.183	S–C	422	368	314	2.48	4.80
DDTT-EP	61.8	2.756	S–S and S–π	385	378	356	2.25	4.81

[a] Degradation temperature (T_{deg}) determined by TGA corresponding to 5% weight loss at 10 °C min^{-1} under nitrogen flow.
[b] Melting temperature (T_m) measured by DSC with a heating rate 10 °C min^{-1} under nitrogen flow.
[c] The maximum values of absorption spectra of 50 nm thick film deposited by vacuum on quartz at room temperature (RT).
[d] E_g estimated from the onset of absorption spectra ($E_g = 1240/\lambda_{onset}$ eV).
[e] HOMO of materials films determined by CV with ferrocene as reference.

orbital (HOMO) obtained from electrochemical cycle voltammeters. As shown in Fig. 1, the absorption maxima are at 305–356 nm, corresponding to the π–π* transition of DTT derivatives. For DP-DTT, DBP-DTT and DDTT-EP, there exhibits another absorption peak at 220–270 nm, corresponding to the absorption of the aryl group, which may illuminate the deviation of the aryl group from the planar of DTT unit. According to the onset of absorption, E_g is estimated about 2.99 eV for DP-DTT, 2.48 eV for DBP-DTT, 2.92 eV for DEP-DTT, and 2.25 eV for DDTT-EP, respectively. To obtain the HOMO levels, these materials were investigated in the film state by electrochemical cyclic voltammetry (CV), except for DP-DTT due to its poor solubility in dichloromethane. All the materials are oxidized quasi-reversibly in the positive potential region. The HOMO levels can be calculated from the onset potential of the oxidative wave. It is unexpected that the HOMO levels of these materials are almost same, which is different to other results [2,7,13]. This abnormal phenomenon may be attributed to the electropositivity of the middle S atom on DTT unit.

3.2. Single crystal structures and transfer integral calculations

The single crystals of DBP-DTT and DDTT-EP were successfully obtained in the process of vacuum sublimation. X-ray diffraction studies of the single crystal structures are shown in Fig. 2, wherein intermolecular interactions

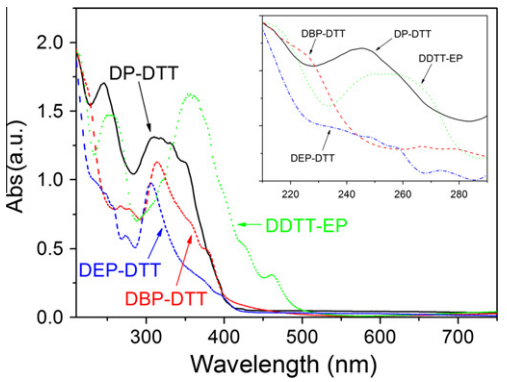

Fig. 1. Film UV–vis absorption spectra of DP-DTT, DBP-DTT, DEP-DTT, and DDTT-EP films deposited on quartz with thickness of 50 nm. The insert is the partial plot of absorption spectra.

are detected for both DBP-DTT and DDTT-EP. The DBP-DTT molecule displays a quasi-bowed shape possessing mirror symmetry as shown in Fig. 2a. The crystal belongs to orthorhombic system and the molecular long axis is *b* axis. The average dihedral angle between the middle thiophene ring (T_m) and the other two thiophene rings (T_s) of DTT unit is about 7.0°. The adjacent two phenyl groups (P_a) is around 13.6°, and the terminal two phenyl groups (P_t) is approximately 21.2°, respectively. Furthermore, only S–C intermolecular interaction is observed as shown in Fig. 2b. The distances between the middle S (S2) atom of DTT unit and two C atoms (C15 and C15A) of neighboring DTT units are both 3.443 Å. The packing mode of DBP-DTT molecules adopt herringbone arrangement with multiple S–H (2.880 Å) intermolecular interactions as shown in Fig. 2c. The herringbone angle and π–π spacing are about 38.2° and 2.183 Å, respectively.

In contrast, the DDTT-EP molecule possesses central symmetry in a "wave" shape as shown in Fig. 2d. The crystal belongs to monoclinic system and the molecular long axis is *a* axis. The average dihedral angles between the middle thiophene ring (T_m) and the other two thiophene rings (T_s) and the phenyl group (P) are about is about 3.3°, 3.3° and 9.7°, respectively. As shown in Fig. 2e, various intermolecular interactions of S (S2)-S (S2A) with a distance of 3.599 Å and S (S2, S2A)-C (C3, C4, C5, C6, C3A, C4A, C5A, C6A) with distances of 3.394 Å, 3.488 Å, 3.428 Å and 3.385 Å, are revealed in the DDTT-EP single crystal structure. Furthermore, DDTT-EP also adopts herringbone arrangement (as shown in Fig. 2f) with a herringbone angle of 61.8° and π–π spacing of 2.756 Å. In addition, it should be noticed that multiple S–H intermolecular interactions also exist among the adjacent molecules as shown in Fig. 1f.

Compared with the single crystal structures of DP-DTT and DEP-DTT as discussed in Ref. [21], it can be concluded that the substitution patterns of the end-capping groups play an important role on the molecular packing and the intermolecular interactions. Table 1 lists the herringbone angle, π–π spacing, and the intermolecular interactions obtained from the single crystal structures. It is evident that the herringbone angle increases and π–π spacing decreases when the intermolecular interaction varies from S–S to S–π and S–C. Furthermore, the middle S atom is electropositive because of the ring opening of DTT unit at the position of middle S atom in the presence of *n*-BuLi [22]. It can therefore be deduced that S–S intermolecular interaction

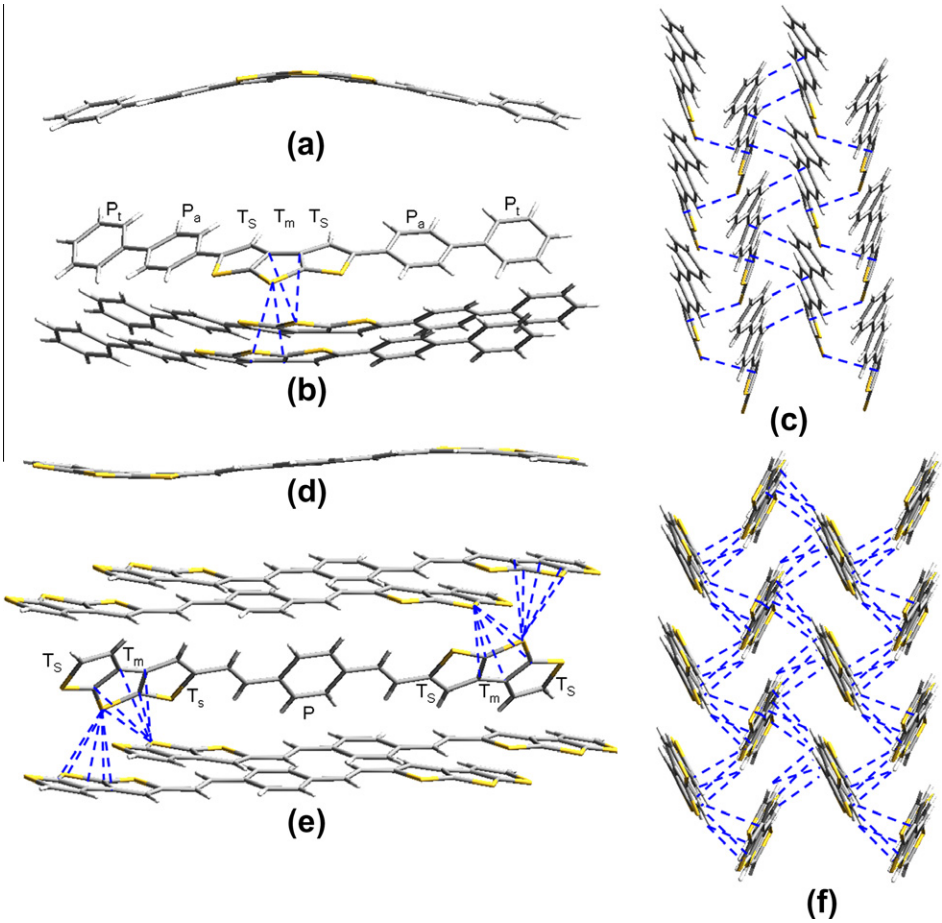

Fig. 2. Intermolecular interactions in the single crystal structures of DBP-DTT (a–c) and DDTT-EP (d–f): (a and d) side-view; (b and e) intermolecular interaction of S–C, S–S, and S–π; (c and f) intermolecular interaction of S–H and crystal packing. The dashed line presents the close contact between atoms.

in DP-DTT is governed by repelling force, which causes the molecules of DP-DTT to adopt a loose arrangement with higher herringbone angle and larger π–π spacing. The electropositivity of the middle S atom weakens when the end-capping aryl groups become planar with respect to the DTT unit, which results in the disappearance of S–S intermolecular interaction and in turn formation of S–C and S–π intermolecular interactions in DBP-DTT and DEP-DTT, respectively. Specially for DDTT-EP, S–S intermolecular interaction does not completely disappear, in spite of the aryl group being almost planar with the DTT unit. At the same time, S–π intermolecular interaction in DDTT-EP may arise from due to the partial conjugation between aryl group and DTT unit. It is very interesting that unsymmetrical substitution of DTT unit leads to the co-existing of S–S and S–π intermolecular interaction in DTT derivatives. Simultaneously, the electropositivity of the middle S atom on DTT unit becomes weak due to the partial conjugation between aryl group and DTT unit. This results in S–S intermolecular interaction in DDTT-EP is weaker than that in DP-DTT, which is evident by the higher distance between the middle S atoms in DDTT-EP (3.599 Å) than that in DP-DTT (3.560 Å). Furthermore, the existence of S–S intermolecular interaction causes the herringbone angle and π–π spacing of DDTT-EP higher than those of DEP-DTT and DBP-DTT, and lower than those of DP-DTT. Therefore, the substitution patterns of aryl groups play an important role on the intermolecular interaction and the existence of S–S intermolecular interaction causes the molecules to adopt a loose arrangement.

According to their single crystal structures, the transfer integrals of charges (holes and electrons) were calculated. Table 2 lists the values of transfer integrals between the neighboring molecular pairs with different hopping pathways as shown in Fig. 3. For the transfer integrals of holes, the highest values emerge when their hopping pathways (*b*

Table 2
Hole and electron transfer integrals (t_h in meV) for the molecular pairs taken from the X-ray crystal structures at different pathways.

Pathway	DP-DTT	DBP-DTT	DEP-DTT	DDTT-EP
a	−14.7	28.2	−65.1	64.3
b	19.1	28.6	−65.2	2.8
c	18.6	−15.5	52.9	−64.1
d	–	−15.5	52.9	64.3
e	–	15.2	−127.6	2.9
f	–	15.5	−127.6	−64.0

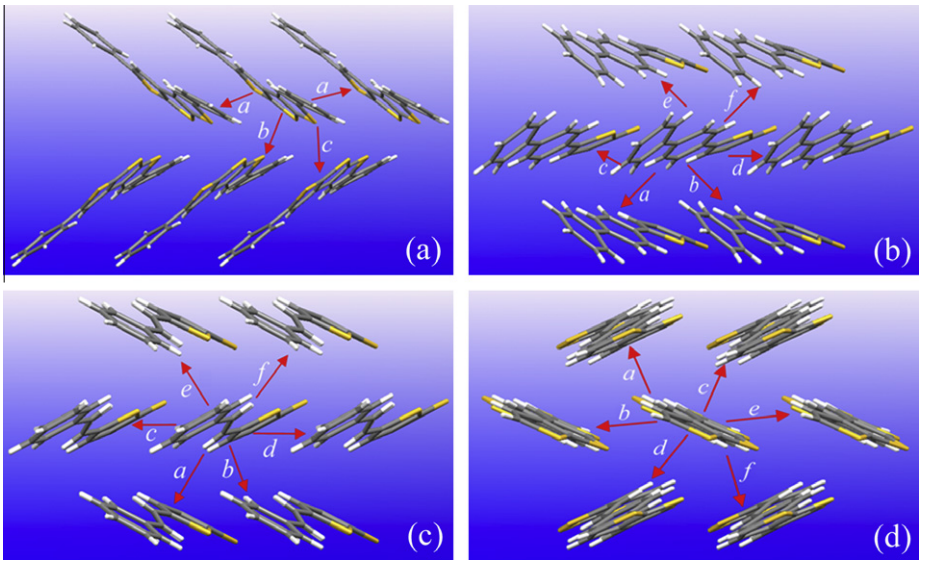

Fig. 3. Charge hopping pathway (*a*, *b*, *c*, *d*, *e* and *f*) of DP-DTT (a), DBP-DTT (b), DEP-DTT (c) and DDTT-EP (d) taken from the single crystal structure for the transfer integral calculation.

and *c* for DP-DTT, *a* and *b* for DBP-DTT, *e* and *f* for DEP-DTT, *a*, *c*, *d* and *f* for DDTT-EP) keep the same direction with the intermolecular interactions. It is obvious that intermolecular interactions benefit the charge carrier transport. As a result, S–π intermolecular interaction in DEP-DTT (*e* and *f* pathway) has a remarkable effect on the charge carrier transport. Furthermore, the charge carrier transport has an efficient pathway (*c* and *d*) at the direction of π–π packing in DEP-DTT due to the condensed molecular arrangement.

3.3. Topographical images and X-ray diffraction patterns

Topographical images of DBP-DTT and DDTT-EP films deposited at different substrate temperature (T_s) were investigated as shown in Fig. 4. All the films possess high

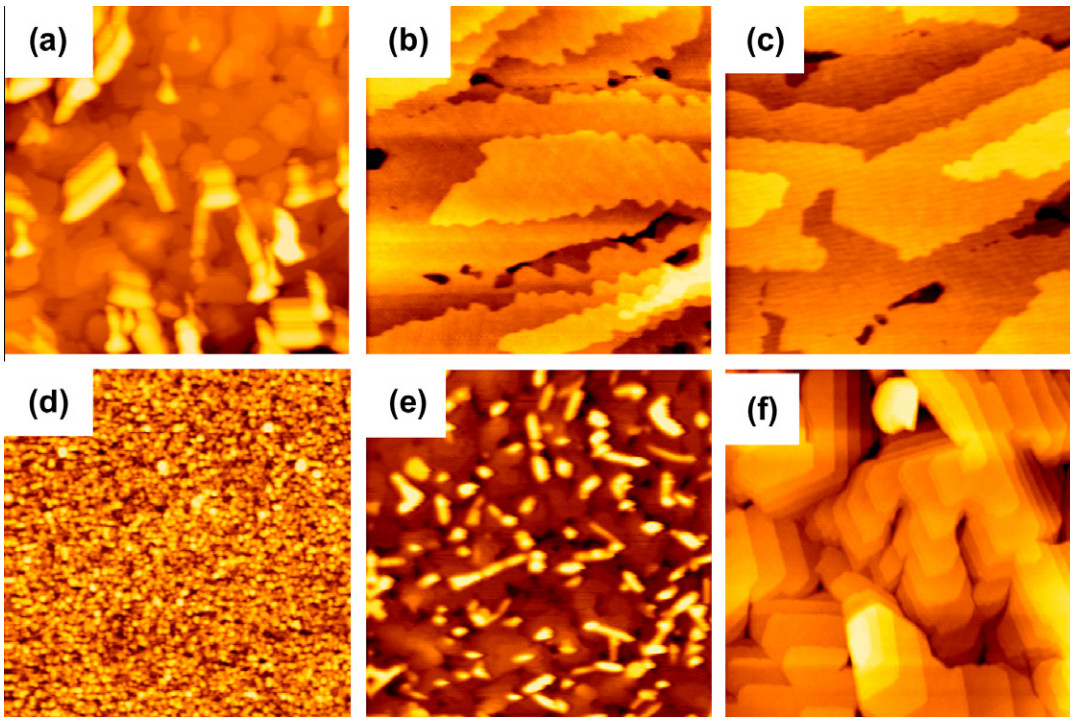

Fig. 4. AFM topographic images of DBP-DTT (*a*, T_s = RT; *b*, T_s = 70 °C; *c*, T_s = 100 °C) and DDTT-EP (*d*, T_s = RT; *e*, T_s = 70 °C; *f*, T_s = 120 °C).

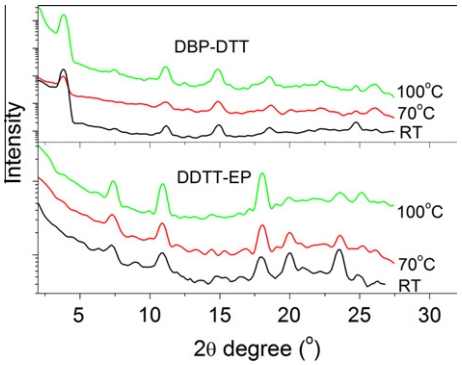

Fig. 5. X-ray diffraction patterns of DBP-DTT and DDTT-EP films deposited at different T_s.

crystalline and are composed of lamellar crystals at high T_s. The average layer spacing is 2.1 nm for DBP-DTT and 2.3 nm for DDTT-EP as shown in Fig. 4c and f, respectively. X-ray diffraction patterns of these materials films deposited at different T_s were also investigated. Fig. 5 shows the typical X-ray diffraction patterns of all films. All the films exhibit a series of peaks with multiple orders of reflection, which indicates that all these films are high crystalline even if they were deposited at T_s of RT. According to their single crystal structures, the indices of crystallographic plane $(0k0)$ for DBP-DTT and $(h00)$ for DDTT-EP were established. The interplanar spacing, calculated according to the Bragg's equation, is about 2.0 nm for DBP-DTT and 2.4 nm for DDTT-EP, which is consistent with that obtained for AFM and the length of the molecular long axis. It can therefore be concluded that the molecular long axes of DBP-DTT and DDTT-EP are almost perpendicular to the substrate. In the process of films growth, the array of the sample molecules would adopt the same way as that in their single crystals due to the intermolecular interactions. Thus it can be concluded that the molecular arrangement in DBP-DTT and DDTT-EP films should be coincident with that in their single crystals.

3.4. Devices performances

OFETs based on these compounds were fabricated at different T_s. Because of the leak current in the devices based on the SiO_2 layer with 300 nm thickness, the properties of the devices fabricated on 500 nm SiO_2 are discussed. Fig. 6 shows the output curves of the devices based on DBP-DTT at T_s of 100 °C and DDTT-EP at T_s of 70 °C. All the devices present typical p-type characteristics and operate in accumulation mode. Table 3 lists the field-effect properties of the devices based on these compounds at different T_s. By optimizing T_s, highest field-effect mobility of 0.52 $cm^2 V^{-1} s^{-1}$ for DBP-DTT, 2.2 $cm^2 V^{-1} s^{-1}$ for DEP-DTT and 0.16 $cm^2 V^{-1} s^{-1}$ for DDTT-EP were obtained, respectively, while DP-DTT does not show field-effect

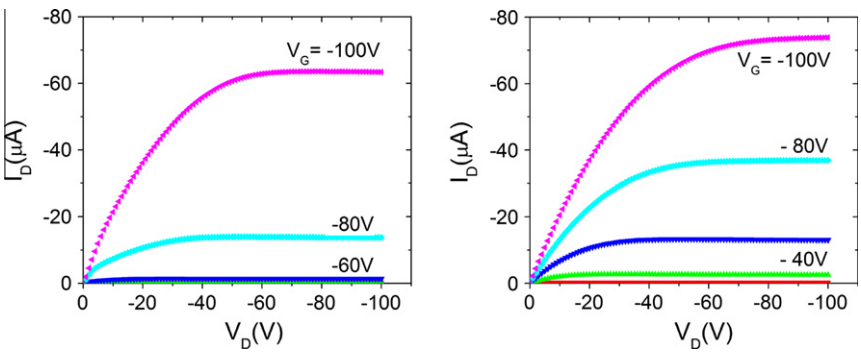

Fig. 6. Output curves of OFETs based on DBP-DTT (T_s = 100 °C) and DDTT-EP (T_s = 70 °C).

Table 3
Field-effect characteristics of OFETs based on DTT derivatives at different T_s.

Materials	T_s (°C)	Mobility[a] ($cm^2 V^{-1} s^{-1}$)	Standard error of mobilities	V_T[a] (V)	I_{on}/I_{off}
DP-DTT	RT	–	–	–	–
	70	–	–	–	–
DBP-DTT	RT	0.25–0.31	0.006	−60 to −64	10^4
	70	0.42–0.52	0.009	−69 to −72	10^4
	100	$6.0–9.3 \times 10^{-4}$	3.1×10^{-5}	−72 to −82	10^4
DEP-DTT	RT	1.2–2.0	0.02	−65 to −68	10^5
	70	1.5–2.2	0.01	−58 to −68	10^5
	100	0.6–1.5	0.01	−64 to −69	105
DDTT-EP	RT	$1.2–1.6 \times 10^{-3}$	1×10^{-4}	−56 to −58	10^2
	70	0.13–0.16	0.004	−30 to −34	10^4
	120	0.10–0.14	0.005	−22 to −27	10^5

[a] All data were extracted from more than ten devices with V_D at −100 V.

behaviors. The previous studies have suggested that S–π intermolecular interaction benefits the carrier transportation [21]. Because of the large area of conductive channel (200 μm * 6000 μm = 1.2E5 μm^2) and the regular arrangement of molecules, the effect of grain boundaries may become similar to the films in the present work. Only from the point of intermolecular interaction, it can be deduced that the mobility varies from none in DP-DTT to 0.52 $cm^2 V^{-1} s^{-1}$ in DBP-DTT and 2.2 $cm^2 V^{-1} s^{-1}$ in DEP-DTT when S–S intermolecular interaction transforms into S–C and S–π intermolecular interaction. But it is unexpected that the mobility of DDTT-EP (0.16 $cm^2 V^{-1} s^{-1}$) is lower than that of DBP-DTT (0.52 $cm^2 V^{-1} s^{-1}$), in spite of the existence of multiple S–π intermolecular interactions and another possible charge transport way provided by S–S intermolecular interaction. Thus, it is clear that the existence of S–S intermolecular interaction in DDTT-EP is unfavorable for mobility improvement, which can be attributed to the loose arrangement. Furthermore, the threshold voltage (V_T) of the devices decreases when S–C intermolecular interaction (in DBP-DTT) turns into S–π intermolecular interaction (in DEP-DTT), and has an evident reduction when the S–S intermolecular interaction forms in DDTT-EP.

4. Conclusions

In summary, a series of DTT derivatives were synthesized. All these materials present field-effect mobility high than 0.1 $cm^2 V^{-1} s^{-1}$. The substitution patterns of aryl groups do not affect the HOMO levels of these materials, but play an important role on the intermolecular interactions. The intermolecular interactions provide another charge hopping pathway and benefit for the charge carrier transport. The formation of S–π intermolecular interaction not only benefits mobility improvement but also redounds to reducing the threshold voltage, while S–S intermolecular interaction contributes no effect on mobility improvement due to its loose arrangements.

Acknowledgements

This work was financially supported by the National Natural Science Foundation of China (50803015 and 20972041), the Program for Changjiang Scholars and Innovative Research Team in University (PCS IRT1126), and Program for Innovation Scientists, Technicians Troop Construction Projects of Henan Province (104100510011), the Opening Project of Key Laboratory for Chemistry of Low-Dimensional Materials of Jiangsu Province and the Cultivation Fund of the Key Scientific Innovation Project of Huaiyin Normal University (11HSGJBZ11). We also thank the Northeast Normal University for providing the computational supports.

Appendix A. Supplementary data

Supplementary data associated with this article can be found, in the online version, at http://dx.doi.org/10.1016/j.orgel.2013.01.002.

References

[1] P.M. Beaujuge, J.M.J. Frechet, J. Am. Chem. Soc. 133 (2011) 20009.
[2] C. Wang, H. Dong, W. Hu, Y. Liu, D. Zhu, Chem. Rev. 112 (2012) 2208.
[3] A. Dodabalapur, Mater. Today 9 (2006) 24.
[4] C.D. Dimitrakopoulos, P.R.L. Malenfant, Adv. Mater. 14 (2002) 99.
[5] H.E.A. Huitema, G.H. Gelinck, J.B.P.H. Putten, K.E. Kuijk, C.M. Hart, E. Cantatore, P.T. Herwig, A.J.J.M. Breemen, D.M. Leeuw, Nature 414 (2001) 599.
[6] A. Tsumura, H. Koezuka, T. Ando, Appl. Phys. Lett. 49 (1986) 1210.
[7] J. Zaumseil, H. Sirringhaus, Chem. Rev. 107 (2007) 1296.
[8] C. Reese, Z. Bao, Mater. Today 10 (2007) 20.
[9] A. Facchetti, Mater. Today 10 (2007) 28.
[10] W. Shao, H. Dong, L. Jiang, W. Hu, Chem. Sci. 2 (2011) 590.
[11] Q. Meng, H. Dong, W. Hu, D. Zhu, J. Mater. Chem. 21 (2011) 11708.
[12] M.L. Tang, Z. Bao, Chem. Mater. 23 (2011) 446.
[13] H. Tian, J. Shi, D. Yan, L. Wang, Y. Yan, F. Wang, Adv. Mater. 18 (2006) 2149.
[14] J.A. Merlo, C.R. Newman, C.P. Gerlach, T.W. Kelley, D.V. Muyres, S.E. Fritz, M.F. Toney, C.D. Frisbie, J. Am. Chem. Soc. 127 (2005) 3997.
[15] H. Wang, F. Zhu, J. Yang, Y. Geng, D. Yan, Adv. Mater. 19 (2007) 2168.
[16] D. Song, H. Wang, F. Zhu, J. Yang, H. Tian, Y. Geng, D. Yan, Adv. Mater. 20 (2008) 2142.
[17] H. Wang, D. Song, J. Yang, B. Yu, Y. Geng, D. Yan, Appl. Phys. Lett. 90 (2007) 253510.
[18] L. Huang, C. Liu, X. Qiao, H. Tian, Y. Geng, D. Yan, Adv. Mater. 23 (2011) 3455.
[19] L. Tan, L. Zhang, X. Jiang, X. Yang, L. Wang, Z. Wang, L. Li, W. Hu, Z. Shuai, L. Li, D. Zhu, Adv. Funct. Mater. 19 (2009) 272.
[20] L. Zhang, L. Tan, Z. Wang, W. Hu, D. Zhu, Chem. Mater. 21 (2009) 1993.
[21] J. Shi, Y. Li, M. Jia, L. Xu, H. Wang, J. Mater. Chem. 21 (2011) 117612.
[22] Z. Wang, C. Zhao, D. Zhao, C. Li, J. Zhang, H. Wang, Tetrahedron 66 (2010) 2168.
[23] Y. Wang, Z. Wang, D. Zhao, Z. Wang, Y. Cheng, H. Wang, Synlett (2007) 2390.
[24] D. Zhao, L. Xu, H. Wang, J. Henan, Univ. Nat. Sci. 37 (2007) 468.
[25] K. Senthilkumar, F.C. Grozema, F.M. Bickelhaupt, L.D.A. Siebbeles, J. Chem. Phys. 119 (2003) 9809.
[26] G. te Velde, F.M. Bickelhaupt, E.J. Baerends, C. Fonseca Guerra, S.J.A. van Gisbergen, J.G. Snijders, T. Ziegler, J. Comput. Chem. 22 (2001) 931.
[27] Y. Zhao, D. Truhlar, Theor. Chem. Acc. 120 (2008) 215.